



# CHORUS

This is the accepted manuscript made available via CHORUS. The article has been published as:

## Reduction in thermal conductivity and tunable heat capacity of inorganic/organic hybrid superlattices

Ashutosh Giri, Janne-Petteri Niemelä, Chester J. Szwejkowski, Maarit Karppinen, and Patrick E. Hopkins

Phys. Rev. B **93**, 024201 — Published 11 January 2016

DOI: [10.1103/PhysRevB.93.024201](https://doi.org/10.1103/PhysRevB.93.024201)

# Reduction in thermal conductivity and tunable heat capacity of inorganic/organic hybrid superlattices

Ashutosh Giri,<sup>1</sup> Janne-Petteri Niemelä,<sup>2</sup> Chester J. Szejewski,<sup>1</sup> Maarit Karppinen,<sup>2</sup> and Patrick E. Hopkins<sup>1,\*</sup>

<sup>1</sup>*Department of Mechanical and Aerospace Engineering,  
University of Virginia, Charlottesville, Virginia 22904, USA*

<sup>2</sup>*Department of Chemistry, Aalto University, FI-00076 Aalto, Finland*

(Dated: December 14, 2015)

We study the influence of molecular monolayers on the thermal conductivities and heat capacities of hybrid inorganic/organic superlattice thin films fabricated via atomic/molecular layer deposition. We measure the cross plane thermal conductivities and volumetric heat capacities of TiO<sub>2</sub>- and ZnO-based superlattices with periodic inclusion of hydroquinone layers via time domain thermoreflectance. In comparison to their homogeneous counterparts, the thermal conductivities in these superlattice films are considerably reduced. We attribute this reduction in the thermal conductivity mainly due to incoherent phonon boundary-scattering at the inorganic/organic interface. Increasing the inorganic/organic interface density reduces thermal conductivity and heat capacity of these films. High temperature annealing treatment of the superlattices results in a change in the orientation of the hydroquinone molecules to a 2D graphitic layer along with a change in overall density of the hybrid superlattice. The thermal conductivity of the hybrid superlattice increases after annealing, which we attribute to an increase in crystallinity.

PACS numbers: 66.70.-f 63.22.-m 68.35.-p 68.37.-d

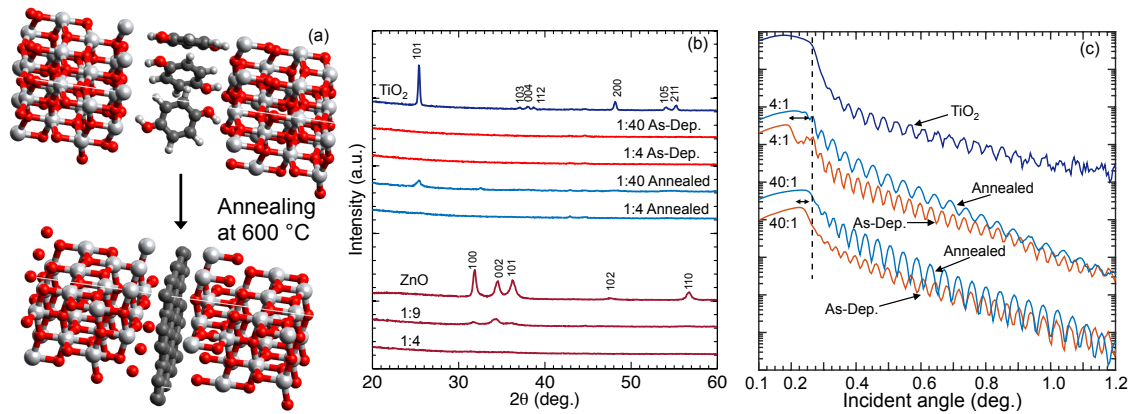


Figure 1. (a) Schematic representation of the TiO<sub>2</sub>-based hybrid structures for the as-deposited and annealed cases. The HQ layers transition into 2D graphitic layers due to the high annealing treatment. (b) Grazing incidence X-ray diffraction (GIXRD) patterns for the control samples and the hybrid films. (c) XRR patterns for the TiO<sub>2</sub> based SLs with  $k:m$  ratio of 1:40 and 1:4, as well as for the purely inorganic TiO<sub>2</sub> film.

20

## I. INTRODUCTION

21 A new class of hybrid inorganic/organic materials grown via a combination of atomic layer deposition (ALD) and molecular  
 22 layer deposition (MLD) have recently garnered much attention due to their ultralow thermal conductivities.<sup>1-3</sup> Integrated with  
 23 their enhanced electrical, optical, magnetic and mechanical properties in comparison to their conventional organic or inorganic  
 24 counterparts, these novel nanomaterials make for attractive candidates for a wide array of applications in nanotechnology.<sup>4-7</sup>  
 25 For example, stemming from the ultra-low thermal conductivity, hybrid superlattice (SL) films have been shown to be ideal  
 26 candidates for energy conversion technologies.<sup>2,3,8</sup> The low thermal conductivities in these SLs have been achieved by the  
 27 inclusion of regularly spaced organic layers in-between thicker inorganic constituents, which drastically reduce phonon transport  
 28 in the cross plane direction.

29 Although plenty of interest has been shown towards understanding thermal transport in organic-based nanocomposites,<sup>9-18</sup>  
 30 there has been limited studies focusing on heat capacity measurements of ALD/MLD grown nanomaterials. Understanding the  
 31 energy storage potential (quantified by the heat capacity,  $C$ ) along with thermal transport efficiency (quantified by the thermal  
 32 conductivity,  $\kappa$ ) is necessary for a complete understanding of energetic processes in hybrid materials.

33 We report on the thermal conductivities and heat capacities of TiO<sub>2</sub>- and ZnO-based SLs with periodic introduction of organic  
 34 layers in-between the thicker inorganic constituents. The thermal conductivities of the hybrid structures are shown to decrease  
 35 with increasing number of organic layers in the SL structure, which is attributed to incoherent phonon boundary scattering at  
 36 the inorganic/organic/inorganic interfaces. The inclusion of the periodic organic layers are also shown to decrease the overall  
 37 heat capacities of these SLs. The effect of high temperature annealing treatment increases the thermal conductivities and heat  
 38 capacities of the TiO<sub>2</sub>-based superlattices. This increase in the thermal conductivities is mainly attributed to enhanced crys-  
 39 tallinity of the inorganic constituents after annealing, whereas, the increase in the heat capacities is mainly due to the increase  
 40 in the density of the SLs due to the transition in orientation of the organic layers as a result of high temperature annealing. This  
 41 demonstrates the ability to control the thermal conductivities and heat capacities of hybrid SLs based on different atomic-scale  
 42 structural mechanisms.

43

## II. EXPERIMENTAL DETAILS

44

### A. Sample fabrication and characterization

45 Hybrid SLs of  $[(\text{TiO}_2)_m(\text{Ti}-\text{O}-\text{C}_6\text{H}_4-\text{O})_{k=1}]_n$  with  $m = 40$  and  $4$  were fabricated on MgO substrates at 210°C via  
 46 the ALD/MLD technique<sup>19</sup> from TiCl<sub>4</sub>, H<sub>2</sub>O and hydroquinone (HQ) precursors (Picosun R-100 ALD reactor) as described in  
 47 detail in our previous reports.<sup>2,20</sup> An illustration of a hybrid SL is shown in Fig. 1a. Additionally,  $[(\text{ZnO})_m(\text{Zn}-\text{O}-\text{C}_6\text{H}_4-\text{O})_{k=1}]_n$   
 48 with  $m = 9$  and  $4$  were also fabricated on Al<sub>2</sub>O<sub>3</sub> substrates to complement our previous experiments, reported in Ref. 3. Along  
 49 with the SL films, control samples of purely ALD grown inorganic TiO<sub>2</sub> and ZnO films were fabricated.

50 Figure 1b shows the characteristic grazing incidence X-ray diffraction (GIXRD) patterns for the films tested in this study. The  
 51 fact that the intensity of the peaks for the as deposited TiO<sub>2</sub>-based SLs are reduced compared to the purely ALD grown TiO<sub>2</sub>

Table I. Thicknesses and densities of the thin films measured via XRR.

Sample	Thickness (nm)	Density (g cm <sup>-3</sup> )
ALD-grown TiO <sub>2</sub>	98.3	3.65
[(TiO <sub>2</sub> ) <sub>m=40</sub> (Ti - O - C <sub>6</sub> H <sub>4</sub> - O-) <sub>k=1</sub> ] <sub>n</sub> (as-deposited)	110.8	2.87
[(TiO <sub>2</sub> ) <sub>m=40</sub> (C) <sub>k=1</sub> ] <sub>n</sub> (annealed)	95.1	3.37
[(TiO <sub>2</sub> ) <sub>m=4</sub> (Ti - O - C <sub>6</sub> H <sub>4</sub> - O-) <sub>k=1</sub> ] <sub>n</sub> (as-deposited)	123.7	1.98
[(TiO <sub>2</sub> ) <sub>m=4</sub> (C) <sub>k=1</sub> ] <sub>n</sub> (annealed)	85.3	2.83
ALD-grown ZnO	154.0	5.4
[(ZnO) <sub>m=9</sub> (Zn - O - C <sub>6</sub> H <sub>4</sub> - O-) <sub>k</sub> ] <sub>n</sub>	93.8	3.3
[(ZnO) <sub>m=4</sub> (Zn - O - C <sub>6</sub> H <sub>4</sub> - O-) <sub>k</sub> ] <sub>n</sub>	82.7	2.4

with anatase phase, suggests that the crystallinity in those samples is hindered due to the inclusion of the HQ layers. In contrast, for the ZnO-based SLs, inclusion of HQ layers for the  $m = 9$  sample does not drastically hinder the peaks in the XRD patterns (that fit the typical ZnO hexagonal wurzite structure). Also, there is negligible change in the position of the peaks, implying that the crystallinity for this sample is fairly conserved. The  $m = 4$  samples for both ZnO and TiO<sub>2</sub>-based SLs are amorphous in nature.

In order to enhance the crystallinity of the TiO<sub>2</sub>-based SLs, the samples were heat-treated at 600°C for 6 hours (Nabertherm GmbH RS 80/500/11). For the  $k:m=1:40$  TiO<sub>2</sub>-based SL (with inorganic period thickness of  $\sim 2$  nm), the high annealing treatment leads to enhanced crystallinity, whereas, for the  $k:m=1:4$  TiO<sub>2</sub>-based SL, GIXRD pattern does not show any change compared to the 1:4 as-deposited SL. Furthermore, the annealing process converts the molecular HQ components to a 2D graphitic layer as depicted in the schematic shown in Fig. 1a. This conversion was confirmed *via* Raman Spectroscopy and further details on the characterization of the carbon content in the fine internal interfaces for these hybrid SLs can be found in our previous report.<sup>2</sup> Note, this annealing treatment does not affect the periodic layering of the SLs as demonstrated by the X-ray reflectivity (XRR; PANanalytical X'Pert Pro MPD diffractometer) patterns with interference maxima due to SL reflections as shown in Fig. 1d of Ref. 2 for the TiO<sub>2</sub>-based SLs with  $k:m=1:200$  and 1:400. However, as the layer spacing is inversely proportional to the XRR angle  $\theta$ , and because the reflected intensity decays exponentially with increasing  $\theta$ , we do not observe the SL reflections for our hybrid films with very small layer spacing ( $k:m=1:4$  and 1:40) as shown in Fig. 1c. In theory, these hybrid films with very small layer spacing should show SL reflections at high  $\theta$  angle. Therefore, we extend the measured  $\theta$  range for these samples and from the observed peaks in the XRR intensity, confirm that the SLs with  $k:m=1:4$  and 1:40 are in fact layered structures.

The small differences in the XRR patterns seen for the as-deposited and annealed samples reveal a reduction in the film thickness and consequent increase in the film densities. The arrows in Fig. 1c. highlight the reduction in the film thickness after annealing that underline the shifts in the critical angle ( $\theta_c$ ) values. The density reduction is expected to mainly stem from the contraction of the organic layers. We estimate the densities from the critical angle values of the XRR patterns.<sup>21</sup> First, the mean electron density values were estimated from  $\rho_e = (\theta_c^2 \pi) / (\lambda^2 r_e)$ , where  $\lambda$  is the X-ray wavelength and  $r_e$  is the classical electron radius. Then, assuming elemental compositions to follow the stoichiometry of [(TiO<sub>2</sub>)<sub>m</sub>(Ti - O - C<sub>6</sub>H<sub>4</sub> - O-)<sub>k</sub>]<sub>n</sub> or [(ZnO)<sub>m</sub>(Zn - O - C<sub>6</sub>H<sub>4</sub> - O-)<sub>k</sub>]<sub>n</sub>, the mean mass densities were obtained from  $\rho_m = (\rho_e A) / (N_A Z)$ , where  $A$  is the average molar mass,  $N_A$  is the Avogadro constant and  $Z$  the average atomic number. The estimated densities along with the measured thicknesses for the thin films are shown in Table I.

## B. Time-domain thermoreflectance

We measure the thermal properties of the samples with the time domain thermoreflectance (TDTR) technique. The details of the experimental procedure as well as the analysis process have been discussed in Refs. 22–24. For this study, we modulate the pump beam at different frequencies and monitor the in-phase ( $V_{in}$ ) and out-of-phase ( $V_{out}$ ) signals of the reflected probe beam with a lock-in amplifier. Prior to TDTR measurements, we metallize the samples with  $\sim 80$  nm of Al transducer, the thickness of which is determined via picosecond acoustics.<sup>25,26</sup>

We analyze the TDTR data with a 3 layer thermal model (layer 1: Al, layer 2: ALD/MLD SL, layer 3: semi-infinite substrate) and simultaneously measure the heat capacities and thermal conductivities of the hybrid SLs. The thermal boundary conductances at the Al/SL film and SL film/substrate interfaces have to be separated from the measurements to correctly predict the intrinsic thermophysical properties of the SL films. To this end, we analyze the sensitivity of the measurements to the various

90 parameters in the thermal model. The sensitivity of the ratio ( $-V_{in}/V_{out}$ ) to a thermophysical quantity is defined by,<sup>27</sup>

$$S_x = \frac{\partial \ln(-V_{in}/V_{out})}{\partial \ln(x)} \quad (1)$$

91 where  $x$  is the thermophysical parameter of interest. Figure 2a and 2b show the calculations of Eq. 1 for the sensitivity of the  
 92 ratio to the various parameters in our 3 layer thermal model for the  $\text{TiO}_2$ -based SL with  $m = 40$  at two different pump modulation  
 93 frequencies ((a) 8.8 MHz and (b) 3.72MHz). The most sensitive parameters are the heat capacity ( $C_{\text{TiO}_2:\text{HQ}}$ ) and thermal  
 94 conductivity ( $\kappa_{\text{TiO}_2:\text{HQ}}$ ) of the hybrid SLs. The fact that the sensitivities are different and dynamic in nature allows us to simulta-  
 95 neously measure  $C_{\text{TiO}_2:\text{HQ}}$  and  $\kappa_{\text{TiO}_2:\text{HQ}}$  as discussed in detail below. The front side interface conductance,  $h_{K,\text{Al}/\text{TiO}_2}$ , and the  
 96 back side interface conductance  $h_{K,\text{TiO}_2/\text{MgO}}$  are measured from separate measurements on the control sample ( $\text{Al}/\text{TiO}_2/\text{MgO}$ ).  
 97 As shown in Fig. 2a and b, the measurements are insensitive to  $h_{K,\text{Al}/\text{TiO}_2}$ , however, a 10% uncertainty in  $h_{K,\text{TiO}_2/\text{MgO}}$  leads  
 98 to a  $\sim 1.2\%$  and  $\sim 2.4\%$  uncertainty in  $\kappa_{\text{TiO}_2:\text{HQ}}$  and  $C_{\text{TiO}_2:\text{HQ}}$  at room temperature for 8.8 MHz frequency, respectively, which  
 99 quantifies this insensitivity.

100 We confirm the measurements for  $h_{K,\text{Al}/\text{TiO}_2}$  and  $h_{K,\text{TiO}_2/\text{MgO}}$  by analyzing the thermoreflectance data for the control  
 101 sample using two different approaches. The first approach analyzes the  $V_{in}$  as well as  $-V_{in}/V_{out}$  separately, as we outline in  
 102 detail elsewhere.<sup>28</sup> The second method utilizes two frequencies to effectively separate the interfacial conductances. At 3.72 MHz  
 103 modulation frequency, we estimate an effective thermal conductivity that considers the front side conductance and the thermal  
 104 conductivity of the hybrid structure as a lumped conductance. We fit the data to the model with this effective conductivity and  
 105 the back side conductance as free parameters. For the higher modulation frequency (8.8 MHz), we fit the data with the free  
 106 parameters as the thermal conductivity of the SL and front side conductance and assume the back side conductance as an input  
 107 parameter determined from the lower modulation frequency. It should be noted that this approach to measuring the front side  
 108 and back side conductances gives agreeable values to the first method outlined in Ref. 28. Uncertainties in the measured thermal  
 109 conductivities and heat capacities of the hybrid SLs are derived from the uncertainties in the input parameters and the sensitivity  
 110 of the 3 layer thermal model to those parameters. We measure a value of  $\kappa = 5.2 \pm 0.5 \text{ W m}^{-1} \text{ K}^{-1}$  for the purely ALD grown  
 111  $\text{TiO}_2$  film, which is in good agreement with the literature value of  $\sim 5.7 \text{ W m}^{-1} \text{ K}^{-1}$  for an Anatase thin film.<sup>29</sup>

112 For a given frequency, the best fit to our TDTR signal (for hybrid SLs with high interfacial densities) can be produced with  
 113 multiple combinations of the heat capacities and thermal conductivities, as shown in the sensitivity contour plots in Fig. 2c for  
 114 a  $k:m=1:4$ , as-deposited  $\text{TiO}_2$ -based SL. The contour plots represent the mean square deviation of the model to the TDTR data  
 115 with the various combinations of  $C$  and  $\kappa$  as input parameters in our 3-layer model.<sup>30</sup> Note, our best fits to the TDTR data are  
 116 usually  $\lesssim 0.02$ . As is clear from the sensitivity contour plot, a wide range of values for  $C$  can produce the best fit in the least  
 117 squares sense for a given frequency. Therefore, to accurately determine  $C$  and  $\kappa$ , we use 3.72 and 8.8 MHz pump modulation  
 118 frequencies that give different sensitivity contour maps for the thermophysical properties (see Fig. 2c). The common set of  
 119 values for  $C$  and  $\kappa$  at these two frequencies shown by the overlap of the best fit values represent our measurements for the hybrid  
 120 multilayers.

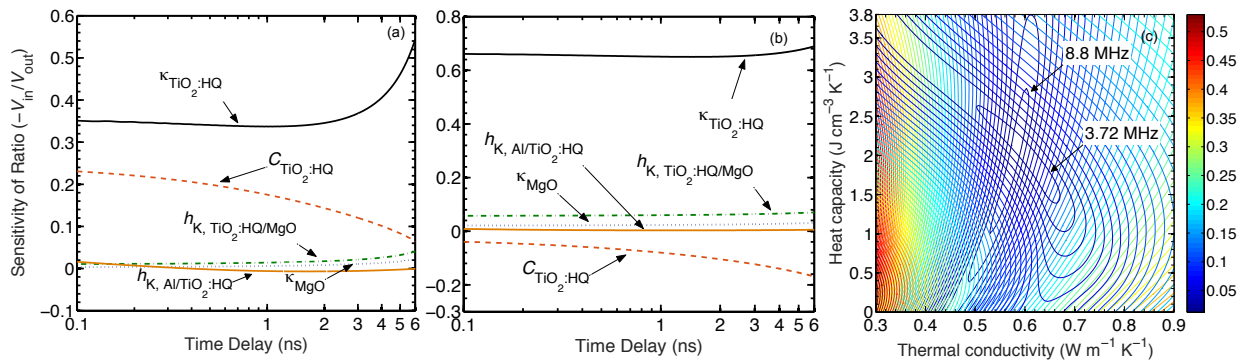


Figure 2. Sensitivities of ratio ( $-V_{in}/V_{out}$ ) to the thermo-physical properties of the As-Dep  $[(\text{TiO}_2)_{m=4}(\text{Ti}-\text{O}-\text{C}_6\text{H}_4-\text{O}-)_{k=1}]_n$  sample as a function of pump-probe time delay at (a) 8.8 MHz pump modulation frequency and (b) 3.72 MHz pump modulation frequency. (c) Sensitivity contour plot showing the interrelationship between thermal conductivity and heat capacity of the As-Dep  $[(\text{TiO}_2)_{m=4}(\text{Ti}-\text{O}-\text{C}_6\text{H}_4-\text{O}-)_{k=1}]_n$  sample at 3.72 MHz and 8.8 MHz pump modulation frequencies.

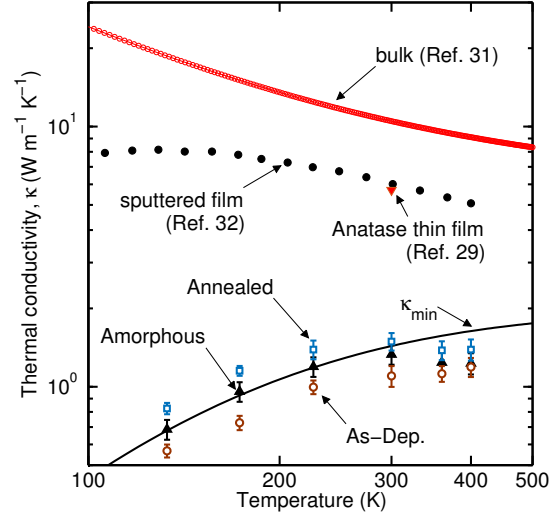


Figure 3. Thermal conductivities of as-deposited and annealed TiO<sub>2</sub>-based  $m = 40$  SLs plotted as a function of temperature. For comparison, the measured thermal conductivities of an ALD grown amorphous TiO<sub>2</sub> film along with the thermal conductivities of bulk, single crystal TiO<sub>2</sub> (Ref. 31), a polycrystalline sputtered film with 17 nm grain size (Ref. 32) and Anatase thin film (Ref. 29) are also shown. The calculated minimum in thermal conductivity for TiO<sub>2</sub> is also shown for comparison.

### III. THERMAL CONDUCTIVITY

Figure 3 shows the measured thermal conductivities for the as-deposited and annealed TiO<sub>2</sub>-based samples with  $m = 40$  as a function of temperature. Two aspects of the results shown in Fig. 3 are worth noting. First, the thermal conductivities measured for the as-deposited and annealed SLs show a large reduction as compared to the sputtered TiO<sub>2</sub> thin films;<sup>32</sup> at room temperature,  $\kappa$  for the as-deposited SL is almost 30% lower than the measured  $\kappa$  for an Anatase thin film (Fig. 3; solid triangle).<sup>29</sup> For comparison, we have also included thermal conductivity of bulk, single crystal Anatase taken from Ref. 31. The reason for the decrease in the thermal conductivities is attributed to incoherent boundary scattering at the inorganic/organic interfaces.<sup>2</sup> The results for the hybrid SLs agree well with the model for the minimum limit to thermal conductivity of TiO<sub>2</sub> (solid black line in Fig. 3).<sup>32,33</sup> For comparison, Fig. 3 also shows the measured  $\kappa$  for an as-deposited amorphous TiO<sub>2</sub> film. Even with the enhancement in crystallinity of the annealed sample, boundary scattering at the inorganic/organic/inorganic interfaces results in the low values for thermal conductivities. In Fig. 3, we have also added the predictions from a minimum thermal conductivity model for a homogeneous amorphous TiO<sub>2</sub> sample. This model assumes that the “mean free paths” of vibrations in the amorphous state are limited to the spacing between the atoms. Therefore, following Ref. 33, the thermal conductivity as a result from random walk between localized oscillators is,

$$\kappa_{\min} = \left(\frac{\pi}{6}\right)^{1/3} k_B n^{2/3} \sum_i v_i \left(\frac{T}{\Theta_i}\right)^2 \int_0^{\Theta_i/T} \frac{x^3 e^x}{(e^x - 1)^2} dx, \quad (2)$$

where the sum is taken over the three sound speeds ( $v_i$ ),  $n$  is the atomic density, and  $\Theta_i = v_i(\hbar/k_B)(6\pi^2 n)^{1/3}$  is the cutoff frequency for each polarization expressed in degrees.<sup>33</sup> For the calculations shown in Fig. 3 (for a homogeneous TiO<sub>2</sub>), the longitudinal and transverse sound speeds are taken from Ref. 34. As is clear from Fig. 3, the predicted minimum in thermal conductivity for TiO<sub>2</sub> agrees very well with our measured values for a homogeneous amorphous TiO<sub>2</sub> thin film and the thermal conductivity can be further lowered below this minimum limit by the inclusion of periodic monolayers of HQ.

The second aspect to note in Fig. 3 is the increase in the thermal conductivities of the hybrid SLs after annealing at 600°C for 6 hours. This can be understood as a consequence of enhanced crystallinity of the inorganic constituents due to the high annealing temperatures. However, the role of the different organic constituents (2D graphitic carbon layers in the annealed samples as compared to the HQ monolayers in the as-deposited samples) might affect the vibrational scattering mechanisms differently at these molecular interfaces. To understand the relative contributions of these two competing effects on thermal conductivity, we compare the results for the annealed and as-deposited samples with  $m = 4$  as reported in our previous work.<sup>2</sup> We measure  $\kappa = 0.62 \pm 0.04 \text{ W m}^{-1} \text{ K}^{-1}$  and  $0.66 \pm 0.04 \text{ W m}^{-1} \text{ K}^{-1}$  for the as-deposited and annealed samples, respectively. For these samples, even with the high annealing treatments, the inorganic constituents are mostly amorphous in nature, as

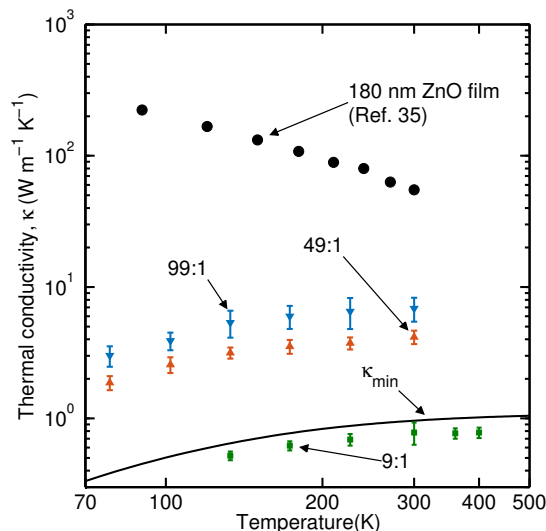


Figure 4. Thermal conductivities of ZnO-based  $m = 9$  SLs along with the thermal conductivities of  $m = 99$  and  $49$  hybrid SLs (Ref. 28), and a  $180$  nm ZnO film (Ref. 35). The calculated minimum in thermal conductivity for ZnO is also shown for comparison.

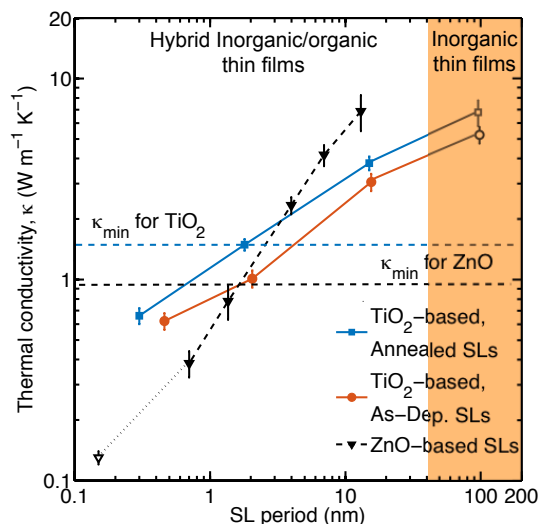


Figure 5. Thermal conductivities of ZnO- and  $\text{TiO}_2$ -based SLs as a function of SL period thickness. The measured thermal conductivity for a  $k:m=1:1$  hybrid film reported in Ref. 1 is also plotted (hollow triangle). The calculated minimum in thermal conductivities for ZnO and  $\text{TiO}_2$  are also shown for comparison. Note, for the case of as-deposited and annealed  $\text{TiO}_2$ , the SL period of  $\sim 100$  nm are for the corresponding purely ALD grown samples with  $k = 0$  (hollow symbols).

148 demonstrated by the GIXRD patterns in Fig. 1. Consequently, the values for the measured thermal conductivities are agreeable  
 149 within uncertainties, suggesting that the role of the organic layers (in these two samples with the same number of organic  
 150 interfaces) in thermal transport are similar; in other words, the orientation of the HQ layer does not affect scattering at the  
 151 inorganic/organic boundary and the resulting vibrational thermal conductivity. Contrary to the  $m = 4$  sample, the crystallinity  
 152 of the  $m = 40$  sample is enhanced after annealing as demonstrated by the increase in the 101 peak (see Fig. 1b) and, therefore,  
 153 the increase in  $\kappa$  is a consequence of enhanced crystallinity and not due to the intrinsic scattering mechanisms in the organic  
 154 layers.

155 Figure 4 shows the measured thermal conductivities for the ZnO-based  $m = 9$  SL as a function of temperature. Along with  
 156 these measurements, we also include the measured thermal conductivities of  $m = 99$  and  $m = 49$  SLs from our previous work.<sup>28</sup>

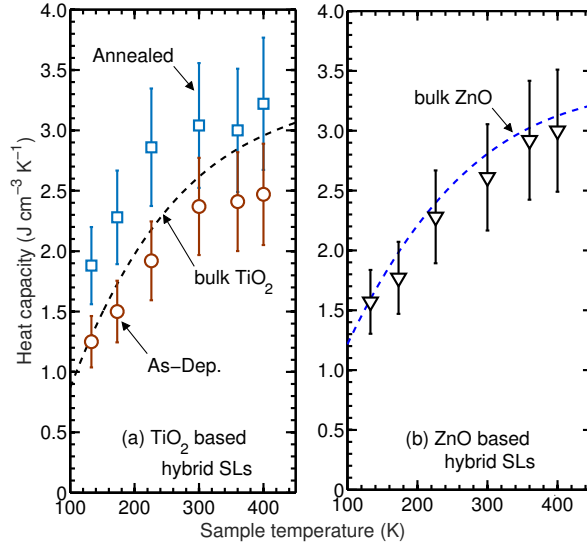


Figure 6. Measured volumetric heat capacities as a function of temperature for (a)  $[(\text{TiO}_2)_{m=40}(\text{Ti}-\text{O}-\text{C}_6\text{H}_4-\text{O})_{k=1}]_n$  and (b)  $[(\text{ZnO})_{m=9}(\text{Zn}-\text{O}-\text{C}_6\text{H}_4-\text{O})_{k=1}]_n$  SLs. The corresponding bulk heat capacities for the inorganic constituents are also shown for comparison.<sup>37,38</sup>

157 Similar to the results for the  $\text{TiO}_2$ -based SLs, the inclusion of HQ monolayers in-between the thicker inorganic constituents is  
 158 shown to drastically reduce the thermal conductivities compared to the measurements of a homogeneous thin ZnO film from  
 159 Ref. 35. We have attributed the reduction in  $\kappa$  for the ZnO-based hybrid SLs as a phonon-boundary scattering limited process  
 160 (by considering the thermal boundary conductance across ZnO/HQ/ZnO interfaces). The scattered phonon energies almost  
 161 perfectly transmit across the organic monolayers (depending on the phonon wavelength), and the scattering within the organic  
 162 layers itself do not contribute significantly to the overall reduction in thermal transport.<sup>28</sup> In comparison to the minimum thermal  
 163 conductivity calculated for ZnO from elastic constants reported in Ref. 36,  $\kappa$  for the  $m = 9$  SL are well below the minimum  
 164 limit, suggesting that the inclusion of periodic HQ layers can severely limit thermal transport in these hybrid structures.

165 We plot the measured thermal conductivities as a function of SL period thickness for the ZnO- and  $\text{TiO}_2$ -based SLs in Fig. 5.  
 166 The results show that as the SL period thickness increases, the thermal conductivities increase monotonically for all the hybrid  
 167 SLs. The drastic increase in  $\kappa$  as a function of SL period thickness of the ZnO-based SLs as compared to the  $\text{TiO}_2$ -based SLs is  
 168 due to the fact that the phonon flux in a ZnO layer is much greater than that in the  $\text{TiO}_2$  layer.<sup>28</sup> Furthermore, the  $m = 4$   $\text{TiO}_2$ -  
 169 based SLs and the  $m = 9$  and 4 ZnO-based SLs demonstrate thermal conductivities that are lower than the theoretical minimum,  
 170 further providing evidence that thermal transport in these SLs are severely limited by the SL period thicknesses. Figure 5  
 171 also includes the thermal conductivity measured *via* TDTR for a ZnO-based ALD/MLD grown thin film with  $k:m=1:1$ .<sup>1</sup> We  
 172 estimate the period spacing for the ZnO layers in their structure to be  $\sim 0.15$  nm, which is a reasonable estimation considering  
 173 that the average growth rate reported in Ref. 1 is 0.15 nm/cycle. Their measured thermal conductivity is in line with the  
 174 decreasing trend in the thermal conductivity with decreasing period spacing for our hybrid samples. With more than an order  
 175 of magnitude difference in the measured thermal conductivities, ALD/MLD grown hybrid films in general demonstrate a wide  
 176 range of tunability in the design of their thermal conductivities.

#### 177 IV. HEAT CAPACITY

178 Figure 6 shows the measured volumetric heat capacities for the  $\text{TiO}_2$ - and ZnO-based SLs as a function of temperature.  
 179 Along with the thermal conductivities, the heat capacities of the  $\text{TiO}_2$ -based SLs increase significantly due to the high annealing  
 180 treatment as shown in Fig. 6a. For comparison, the bulk heat capacities of  $\text{TiO}_2$  are also shown.<sup>38</sup> As expected, the heat capacities  
 181 of the as-deposited SL are close to the values for the bulk heat capacities due to the fact that the fraction of the organic component  
 182 in the SL film is relatively small (the SL is fabricated with 40 ALD cycles for every 1 MLD cycle). Similarly, the measured heat  
 183 capacities for the ZnO-based sample (with  $m = 9$ ) agree very well with the bulk ZnO heat capacities (Fig. 6b).<sup>37</sup>

184 To understand the effect of higher fractions of organic constituents on the heat capacity of the hybrid SLs, we compare the  
 185 results for the SLs with varying number of organic monolayers as a function of their densities in Fig. 7a. The conversion from

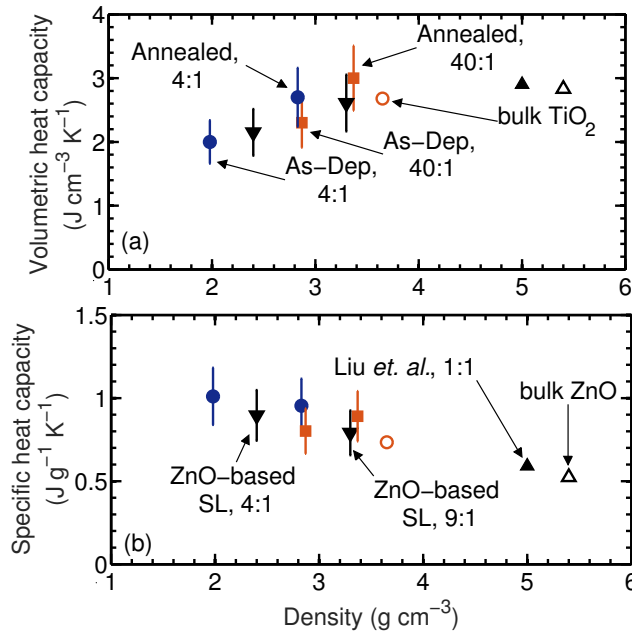


Figure 7. (a) Volumetric heat capacities of the TiO<sub>2</sub>- and ZnO-based thin films plotted as a function of density along with the values of bulk heat capacities for the corresponding inorganic constituents. (b) Specific heat capacities plotted as a function of density. In these plots, the data are designated as follows: TiO<sub>2</sub> (circles), ZnO (triangles), corresponding bulk (open symbol), ALD/MLD SLs (closed symbols). For comparison, the heat capacity measured by Liu *et. al.*<sup>1</sup> for a  $k:m=1:1$  ZnO-based hybrid film is also plotted in the figures.

186 a HQ monolayer to a 2D graphitic layer results in the decrease of the thicknesses of the annealed samples, as mentioned earlier  
 187 (Fig. 1). As a result, the densities of the annealed samples increase considerably (as determined from XRR measurements of the  
 188 thin films). Since the volumetric heat capacity of a substance is directly proportional to mass density, therefore, the volumetric  
 189 heat capacity plotted in Fig. 7a increases monotonically for the as-deposited samples as the density increases. The inclusion of  
 190 more HQ in the SLs decreases the volumetric heat capacity in general due to the reduction in density with higher MLD cycles.  
 191 However, the volumetric heat capacities of the annealed samples (with the 2D graphitic layers) are greater than the as-deposited  
 192 samples as well as that of the corresponding inorganic bulk constituent for the TiO<sub>2</sub> SLs, as mentioned in the previous paragraph.

193 Figure 7b shows the measured specific heat capacities of the materials calculated by dividing the measured volumetric heat  
 194 capacities by their respective measured mass densities (hence, we define the specific heat capacity based on mass, where the  
 195 specific heat capacity,  $c$ , is given by  $c = C/\rho$ , where  $\rho$  is the mass density). As is expected, the specific heat capacities of the  
 196 hybrid SLs deviates from the value of the bulk inorganic constituent as the number of organic monolayer increases. At room  
 197 temperature, the specific heat of the as-deposited TiO<sub>2</sub>- and ZnO-based SLs with  $m = 4$  is closer to the value of the organic  
 198 counterpart, i.e., poly-phenylene oxide ( $1.204 \text{ J g}^{-1} \text{ K}^{-1}$ ). Whereas, the specific heat capacities of the SLs with  $m = 40$  and  
 199  $m = 9$  for the TiO<sub>2</sub>- and ZnO-based SLs, respectively, approach the value of their corresponding inorganic constituents. Unlike,  
 200 the change in the volumetric heat capacities after the high annealing treatment, the specific heat of the annealed SLs show  
 201 good agreement within uncertainties with their as-deposited counterparts (even though the densities increase with annealing).  
 202 In Fig. 7b, we have also included the measured specific heat of a  $k:m=1:1$  ZnO-based hybrid sample reported in Ref. 1 (with  
 203 a density of  $5 \text{ g m}^{-3}$ ). Their result matches the decreasing trend in the measured specific heat with increasing mass density as  
 204 with our hybrid multilayers.

## 205 V. SUMMARY

206 In summary, we have measured the thermal conductivities and heat capacities of TiO<sub>2</sub>- and ZnO-based hybrid SLs with  
 207 periodic organic layers between the inorganic constituents. The inclusion of organic layers is shown to drastically reduce the  
 208 thermal conductivities of these SLs. Furthermore, the thermal conductivities of these hybrid SLs are shown to scale linearly with  
 209 increasing period thickness, suggesting that boundary scattering at the inorganic/organic/inorganic interface dominates the heat  
 210 transfer in these structures. Similarly, the inclusion of organic layers are also shown to decrease the heat capacities. The effect  
 211 of high temperature annealing treatment on the TiO<sub>2</sub>-based SLs is shown to increase both the thermal conductivities and heat

212 capacities. The increase in thermal conductivities due to annealing is attributed to enhanced crystallinity (not due to any intrinsic  
 213 vibrational properties of the organic layer), whereas, the increase in heat capacities is attributed to the increase in the densities  
 214 of the samples.

## 215 ACKNOWLEDGEMENT

216 P.E.H appreciates support from the United States Army Research Office (W911NF-13-1-0378). M.K appreciates support from  
 217 the European Research Council under the European Union's Seventh Framework Programme (FP/2007-2013)/ERC Advanced  
 218 Grant Agreement (No. 339478).

- 
- 219 \* phopkins@virginia.edu
- 220 <sup>1</sup> J. Liu, B. Yoon, E. Kuhlmann, M. Tian, J. Zhu, S. M. George, Y.-C. Lee, and R. Yang, *Nano Letters* **13**, 5594 (2013).
- 221 <sup>2</sup> J.-P. Niemelä, A. Giri, P. E. Hopkins, and M. Karppinen, *J. Mater. Chem. A* **3**, 11527 (2015).
- 222 <sup>3</sup> T. Tynell, A. Giri, J. Gaskins, P. E. Hopkins, P. Mele, K. Miyazaki, and M. Karppinen, *J. Mater. Chem. A* **2**, 12150 (2014).
- 223 <sup>4</sup> B. H. Lee, B. Yoon, V. R. Anderson, and S. M. George, *The Journal of Physical Chemistry C* **116**, 3250 (2012).
- 224 <sup>5</sup> S. M. G. B. Yoon, B. H. Lee, *ECS Trans.* **41** (2011).
- 225 <sup>6</sup> B. Yoon, B. H. Lee, and S. M. George, *The Journal of Physical Chemistry C* **116**, 24784 (2012).
- 226 <sup>7</sup> T. Tynell, I. Terasaki, H. Yamauchi, and M. Karppinen, *J. Mater. Chem. A* **1**, 13619 (2013).
- 227 <sup>8</sup> J. Carrete, N. Mingo, G. Tian, H. Ögren, A. Baev, and P. N. Prasad, *The Journal of Physical Chemistry C* **116**, 10881 (2012).
- 228 <sup>9</sup> W.-L. Ong, S. M. Rupich, D. V. Talapin, A. J. H. McGaughey, and J. A. Malen, *Nat Mater* **12**, 410 (2013).
- 229 <sup>10</sup> W.-L. Ong, S. Majumdar, J. A. Malen, and A. J. H. McGaughey, *The Journal of Physical Chemistry C* **118**, 7288 (2014).
- 230 <sup>11</sup> M. D. Losego, I. P. Blitz, R. A. Vaia, D. G. Cahill, and P. V. Braun, *Nano Letters* **13**, 2215 (2013).
- 231 <sup>12</sup> M. D. Losego, M. E. Grady, N. R. Sottos, D. G. Cahill, and P. V. Braun, *Nat Mater* **11**, 502 (2012).
- 232 <sup>13</sup> S. Majumdar, J. A. Sierra-Suarez, S. N. Schiffres, W.-L. Ong, I. C. Fred Higgs, A. J. H. McGaughey, and J. A. Malen, *Nano Letters* **15**,  
 233 2985 (2015).
- 234 <sup>14</sup> J. C. Duda, P. E. Hopkins, Y. Shen, and M. C. Gupta, *Phys. Rev. Lett.* **110**, 015902 (2013).
- 235 <sup>15</sup> J. P. Feser, E. M. Chan, A. Majumdar, R. A. Segalman, and J. J. Urban, *Nano Letters* **13**, 2122 (2013).
- 236 <sup>16</sup> Y. Jin, C. Shao, J. Kieffer, M. L. Falk, and M. Shtein, *Phys. Rev. B* **90**, 054306 (2014).
- 237 <sup>17</sup> Y. Jin, C. Shao, J. Kieffer, K. P. Pipe, and M. Shtein, *Journal of Applied Physics* **112**, 093503 (2012).
- 238 <sup>18</sup> Y. Jin, A. Yadav, K. Sun, H. Sun, K. P. Pipe, and M. Shtein, *Applied Physics Letters* **98**, 093305 (2011).
- 239 <sup>19</sup> P. Sundberg and M. Karppinen, *Beilstein Journal of Nanotechnology* **5**, 1104 (2014).
- 240 <sup>20</sup> J.-P. Niemelä and M. Karppinen, *Dalton Trans.* **44**, 591 (2015).
- 241 <sup>21</sup> V. Holý, U. Pietsch, and T. Baumbach, *High-Resolution X-Ray Scattering from Thin Films and Multilayers*, p. 127. (Springer Berlin  
 242 Heidelberg, Berlin, 1999).
- 243 <sup>22</sup> D. G. Cahill, *Review of Scientific Instruments* **75**, 5119 (2004).
- 244 <sup>23</sup> A. J. Schmidt, X. Chen, and G. Chen, *Rev Sci Instrum* **79**, 114902 (2008).
- 245 <sup>24</sup> P. E. Hopkins, J. R. Serrano, L. M. Phinney, S. P. Kearney, T. W. Grasser, and C. T. Harris, *Journal of Heat Transfer* **132**, 081302 (2010).
- 246 <sup>25</sup> G. Tas and H. J. Maris, *Phys. Rev. B* **49**, 15046 (1994).
- 247 <sup>26</sup> C. Thomsen, J. Strait, Z. Vardeny, H. J. Maris, J. Tauc, and J. J. Hauser, *Phys. Rev. Lett.* **53**, 989 (1984).
- 248 <sup>27</sup> R. M. Costescu, M. A. Wall, and D. G. Cahill, *Phys. Rev. B* **67**, 054302 (2003).
- 249 <sup>28</sup> A. Giri, J.-P. Niemelä, T. Tynell, J. T. Gaskins, B. F. Donovan, M. Karppinen, and P. E. Hopkins, *In Review* (2015).
- 250 <sup>29</sup> C. Tasaki, N. Oka, T. Yagi, N. Taketoshi, T. Baba, T. Kamiyama, S. ichi Nakamura, and Y. Shigesato, *Japanese Journal of Applied Physics*  
 251 **51**, 035802 (2012).
- 252 <sup>30</sup> J. P. Feser and D. G. Cahill, *Review of Scientific Instruments* **83**, 104901 (2012).
- 253 <sup>31</sup> Y. S. Touloukian, R. W. Powell, C. Y. Ho, and P. G. Klemens, *Thermophysical Properties of Matter - The TPRC Data Series. Volume 2.*  
 254 *Thermal Conductivity - Nonmetallic Solids*, Vol. 2 (IFI/Plenum, New York, 1970).
- 255 <sup>32</sup> S.-M. Lee, D. G. Cahill, and T. H. Allen, *Phys. Rev. B* **52**, 253 (1995).
- 256 <sup>33</sup> D. G. Cahill, S. K. Watson, and R. O. Pohl, *Phys. Rev. B* **46**, 6131 (1992).
- 257 <sup>34</sup> Y. Ding and B. Xiao, *Computational Materials Science* **82**, 202 (2014).
- 258 <sup>35</sup> J. Alvarez-Quintana, E. Martínez, E. Pérez-Tijerina, S. A. Pérez-García, and J. Rodríguez-Viejo, *Journal of Applied Physics* **107**, 063713  
 259 (2010).
- 260 <sup>36</sup> J. Serrano, F. Manjón, A. Romero, A. Ivanov, M. Cardona, R. Lauck, A. Bosak, and M. Krisch, *Phys. Rev. B* **81**, 174304 (2010).
- 261 <sup>37</sup> O. Madelung, U. Rössler, and M. Schulz, "Landolt-börnstein - group iii condensed matter," in *II-VI and I-VII Compounds; Semimagnetic*  
 262 *Compounds*, Vol. 41B (Springer Berlin Heidelberg, 1999) pp. 1–5.
- 263 <sup>38</sup> Z.-G. Mei, Y. Wang, S.-L. Shang, and Z.-K. Liu, *Inorganic Chemistry* **50**, 6996 (2011).